Journal of Luminescence 224 (2020) 117286

Contents lists available at ScienceDirect

Journal of Luminescence

journal homepage: http://www.elsevier.com/locate/jlumin

Structural, optical and dosimetric characterization of $CaSO_4$:Tb, $CaSO_4$:Tb, Ag and $CaSO_4$:Tb,Ag(NP)

Anderson M.B. Silva [a], Danilo O. Junot [b], Linda V.E. Caldas [b], Divanizia N. Souza [a,*]

[a] Departamento de Física,Universidade Federal de Sergipe, DFI/UFS, Av. Marechal Rondon, S/N, 49100-000, São Cristóvão, SE, Brazil
[b] Instituto de Pesquisas Energéticas e Nucleares, Comissão Nacional de Energia Nuclear, IPEN/CNEN-SP, Av. Prof. Lineu Preste, 2242, 05508-000, São Paulo, SP, Brazil

ARTICLE INFO

Keywords:
Dosimetry
Thermoluminescence
Optically stimulated luminescence
Structure properties
Optical properties
$CaSO_4$:Tb,Ag

ABSTRACT

The proposal of this work was to produce and characterize $CaSO_4$ crystals doped with terbium and silver nanoparticles for use in thermoluminescent (TL) and optically stimulated luminescent (OSL) dosimetry. The crystalline structure, morphology and optical properties of the phosphors were characterized by X-ray diffraction (XRD), Raman spectroscopy, Fourier transform infrared spectroscopy, scanning electron microscopy, and photoluminescence. The viability of the slow evaporation route used in the production was confirmed. The silver nanoparticles (Ag(NPs)) were prepared by the method proposed by Lee and Meisel and characterized by XRD and visible absorption spectroscopy (UV–Vis). The composites were obtained from the addition of Teflon to the phosphors. Through the analyses, it was observed that the presence of silver nanoparticles slightly increases the intensity of the emission of the phosphor and shifts the dosimetric TL peak from 185 °C to 310 °C, at a heating rate of 10 °C/s. The samples presented a typical exponential OSL decay curve with a very slow component ($\tau_3 \geq$ 152 s) that indicates that the traps have a low photoionization cross-section for blue LEDs. $CaSO_4$:Tb,Ag(NP) presented a higher sensitivity to radiation than $CaSO_4$:Tb,Ag. The lowest detectable dose (LDD) and the fading of the TL signal of the composites were also evaluated. All samples presented a luminescent signal reproducible and linear, with TL and OSL responses proportional to the absorbed doses in the range of 169 mGy to 10 Gy.

1. Introduction

In order to measure the ionizing radiation, the use of a radiation detector is necessary. Among the available detectors, solid-state dosimeters are widely employed in personal, environmental and clinical dosimetry, with use of techniques such as thermoluminescence and optically stimulated luminescence (OSL). The calcium sulphate is one of the most investigated thermoluminescent (TL) materials to date. It revealed excellent TL properties, appropriate for radiation dosimetry application, doped with several elements [1–6]. Dysprosium and Thulium doped $CaSO_4$ ($CaSO_4$:Dy and $CaSO_4$:Tm) are among the most used materials in routine dosimetry, they present a wide range of linearity of TL dose response to ionizing radiation [4].

Recent studies have proposed the incorporation of new elements as codopants of $CaSO_4$ [7–13]. Junot et al. [10,14] observed that the incorporation of silver into $CaSO_4$:Eu enables more intense TL emissions than in the silver-free material. The increase in the emission intensities was even more expressive (about 5 times higher) when silver was incorporated as a codopant in the form of nanoparticles ($CaSO_4$:Eu,Ag). In another study, Junot et al. [6] produced $CaSO_4$:Tb, Eu crystals and found that this material has excellent dosimetric properties, such as high sensitivity and minimum detectable dose in the order of micrograys.

In the last years, researches have shown that $CaSO_4$ can also be used in the OSL technique, which increases the importance of this material in the field of radiation dosimetry [15–19].

Bahl et al. [20] studied $CaSO_4$:Mn and found that this material shows good OSL characteristics useful for the dosimetry of low doses from beta rays and high doses from gamma radiation. Apart from its high sensitivity, this material has shown excellent reusability characteristics and the dose response was found to be linear in the employed dose ranges. In another study, the dosimetric properties of $CaSO_4$:Eu dosimeter were also checked by Guckan et al. [17]; they observed a high-sensitivity OSL, minimum detectable dose value of ~1 mGy, a reproducible luminescent signal, fading lower than 10% for monitoring periods up of 28 days, and appropriate thermal stability for dosimetry.

Taking into account that there are no reports of dosimetric characterization of $CaSO_4$ doped with terbium and silver, the purpose of this work was to produce and characterize crystals of $CaSO_4$:Tb and $CaSO_4$:

* Corresponding author.
E-mail address: divanizi@ufs.br (D.N. Souza).

https://doi.org/10.1016/j.jlumin.2020.117286
Received 12 December 2019; Received in revised form 12 March 2020; Accepted 9 April 2020
Available online 12 April 2020

Tb, Ag in order to compare these materials, mainly regarding the luminescent response through TL and OSL techniques, for application in radiation dosimetry. Silver was incorporated into the matrix in the form of silver oxide (Ag_2O) and silver nanoparticle (Ag(NP)).

2. Experiment

2.1. Sample preparation

Primarily, the preparation of the silver nanoparticles, Ag(NPs), was performed through the synthesis process proposed by Lee and Meisel [21], which is based on the chemical reduction of silver ions ($AgNO_3$) (Neon, 99.8%) using sodium citrate ($Na_3C_6H_5O_7{\cdot}2H_2O$) (Neon, 99.6%) as reducing and stabilizing agent.

By means of the slow evaporation route, improved by Junot et al. [6], $CaSO_4$:Tb, $CaSO_4$:TbAg, and $CaSO_4$:Tb,Ag(NP) crystals were produced. The production process was based on the mixture of calcium carbonate ($CaCO_3$) (Merck, 99%), sulfuric acid (H_2SO_4) (Vetec, 95–99%), terbium oxide (Tb_4O_7) (Alfa Aesar, 99.9%) and silver oxide (Ag_2O) (Sigma-Aldrich, 99%) or silver nanoparticles (Ag(NPs)) for samples with a second doping. Initially, the terbium ion was incorporated into the matrix in the proportions of 0.01 mol%, 0.05 mol% and 0.1 mol%. A concentration optimization was carried out taking into account the most intense TL/OSL emission, obtained for a 0.1 mol% concentration. Keeping fixed the dopant concentration, the effect of silver oxide and silver nanoparticle as codopants was also evaluated for concentrations of 0.01 mol %, 0.05 mol% and 0.1 mol%. The optimization resulted in concentrations of 0.01 mol% and 0.1 mol% for the silver oxide and silver nanoparticle, respectively. The samples used in this work were produced with the optimized concentrations.

For each material, the solution of $CaSO_4$+H_2SO_4+dopants, resulting from the mixture, was introduced into a volumetric flask and placed on a heating blanket at 375 °C until all the acid evaporated. Subsequently, crystals adhered to the wall of the flask were extracted and transferred to a beaker, undergoing a series of washes with distilled water at room temperature and at 100 °C, alternately, until the solution pH was around 6. The crystals were then macerated and sifted, being used the grains with diameters between 75 μm and 150 μm. The resulting powder was calcined for 1 h at 600 °C. After calcination, pellets were produced by adding 50% polytetrafluoroethylene (Teflon) in mass to the $CaSO_4$ crystals, and pressing under a uniaxial pressure of 0.5 tons during 10 s. After pressing, they were sintered at 450 °C for 1 h. For each pellet, (40 ± 1) mg of the phosphorous + Teflon powder mixture was compacted into a sample of 6 mm in diameter and around 1 mm in thickness. Teflon (DuPont) is a branched polymer, whose chemical formula contains carbon and fluorine [22]. Quite inert and stable, it does not corrode and does not react with other chemicals, being widely used as a binder in the production of TL dosimeters. It offers greater resistance and cohesion to the pellets obtained as a final product. D'Amorim et al. [22] reported that this polymer only shows a detectable TL signal for doses above 7 Gy.

2.2. Sample characterization

In order to confirm the formation of the Ag(NPs), UV–Vis absorption analyses were performed using the spectrophotometer Agilent Cary 100 Scan (Varian), with a scanning range from 300 nm to 800 nm.

X-ray diffraction (DRX) measurements were performed at a Rigaku diffractometer (RINT 2000/PC), using Cu Kα radiation, with the x-ray tube operating at 40 kV and 30 mA, in the continuous scanning mode from 20° up to 80°, in steps of 0.05°/min. Scanning electron microscopy (SEM) images were obtained using a JEOL model JCM-5700 scanning electron microscope. The Fourier transform infrared spectroscopy (FTIR) absorption spectra of the composites in the 500–4000 cm^{-1} spectral range were obtained on a spectrophotometer FTIR-ATR model IR Prestige-21 from Shimadzu. The IR absorption measurements were performed using the KBr pellet technique.

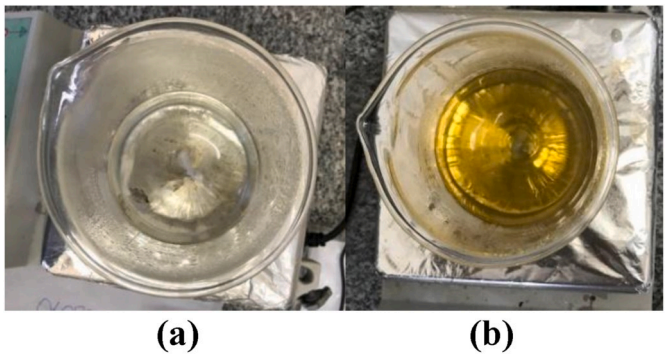

Fig. 1. Visual aspect of the silver nanoparticle solutions, (a) prior to the addition of $AgNO_3$, (b) after the addition step of the reducing agent.

Raman spectra were recorded with a model dispersive Raman spectrometer manufactured by Bruker® Senterra Optik®, using a diode laser of 780 nm wavelength. For these analyses, an objective lens 20 xA, a laser power of 100 mW and the spectral range of 200–1500 cm^{-1} were used, thereby providing the main vibration modes of the composites. The photoluminescence spectra were performed using a JASCO FP8600 spectrofluorometer.

TL and OSL analyses were performed on a Risø TL/OSL reader (Risø National Laboratory, Denmark) immediately after the irradiations, except for the fading measurements, in which the samples were read up to 30 days after irradiation. In the TL/OSL reader a Hoya U-340 filter was used with transmission peak (~80%) at 340 nm and window centered at ~365 nm [23]. The samples were irradiated with the $^{90}Sr/^{90}Y$ beta source at a dose rate of 81.6 mGy/s of the Risø TL/OSL reader. TL emission curves were obtained using a heating rate of 10 °C/s. In order to carry out measurements of the TL emission spectra, a high-resolution spectrometer from Ocean Optics was coupled in place of the photomultiplier. For the OSL measurements, the continuous wave stimulation of blue LEDs with peak emission at 470 nm was employed. After the TL/OSL measurements, the pellets were thermally treated at 400 °C for 2 h, for reutilization.

TL kinetic parameters and glow curve deconvolutions were obtained by means of the Computerized Glow Curve Deconvolution (CGCD) method, using the free GlowFit software. The GlowFit is a program for deconvoluting first order kinetic TL glow-curves. It is based on the first order kinetics model [24]. In the program report, a parameter describing

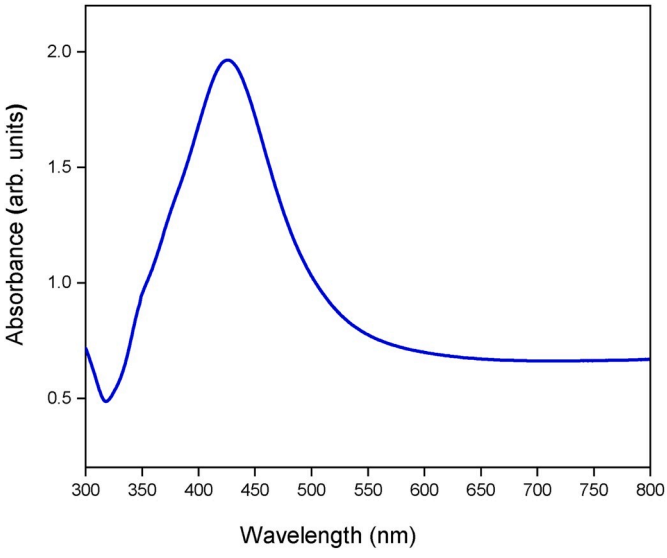

Fig. 2. Absorption spectrum in the UV–Vis region of Ag(NPs) synthesized with sodium citrate in aqueous medium.

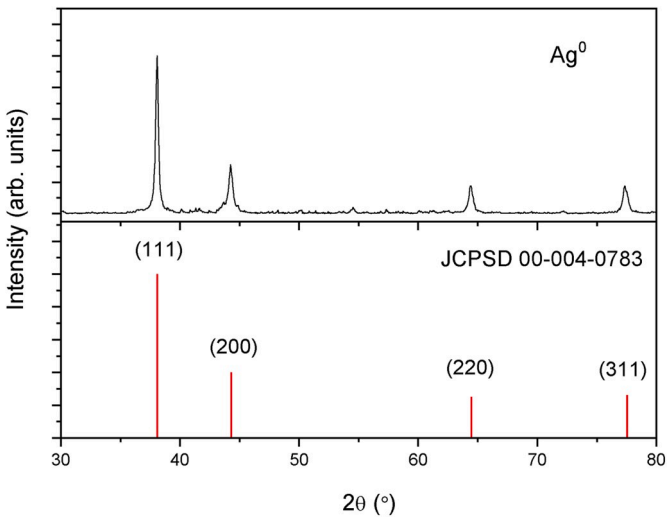

Fig. 3. X-ray diffraction of the silver nanoparticles used as codopant in the $CaSO_4$ matrix and the crystallographic pattern.

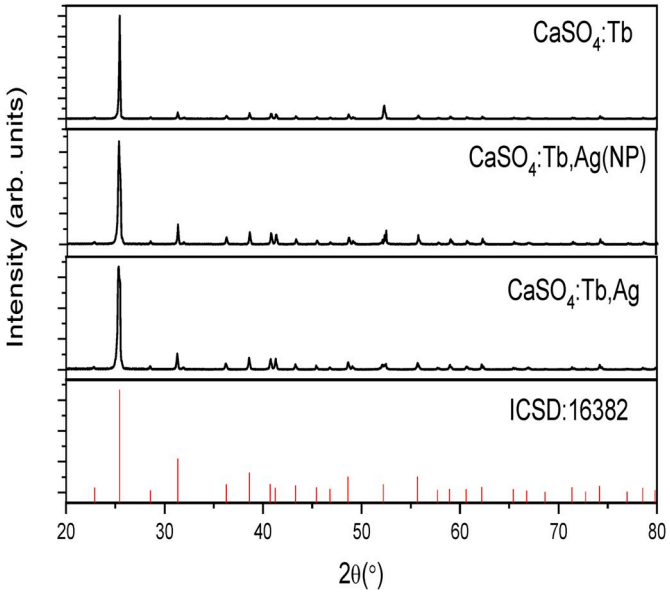

Fig. 4. X-Ray powder diffraction of $CaSO_4$:Tb, $CaSO_4$:Tb,Ag(NP) and $CaSO_4$:Tb, Ag, presented along with the crystallographic pattern.

the fitting quality, called Figure of Merit (FOM), is presented:

$$FOM(\%) = \frac{\sum_i |y_i - y(x_i)|}{\sum_i y_i} * 100\%$$

where y_i is the content of the channel and y (x_i) is the value of fitting function in the middle of the channel.

All results in this work represent the average of at least three different measurements aiming to minimize the uncertainties.

3. Results and discussion

3.1. Characterization of Ag(NPs)

The Ag(NPs) formation was confirmed throughout the synthesis process by observing the change in coloration of the colorless silver nitrate solution (Fig. 1a) to amber yellow (Fig. 1b) moments after addition of the reducing agent. The difference in staining indicates the reduction of Ag^+ ions to Ag^0 and the formation of nanoparticles [25].

The absorption spectrum in UV–Vis (Fig. 2) shows a Plasmon resonance band characteristic of silver nanoparticles, with a maximum around 425 nm, indicating the presence of spherical or approximately spherical nanoparticles [26]. The wide wavelength range of this band indicates a large dispersion of shape and size of the nanoparticles [27].

Fig. 3 shows the X-ray diffraction pattern of the silver powdered nanoparticles. The X-ray diffraction peaks at approximately 38.15°, 44.32°, 64.49° and 77.55° are in accordance with the planes (111), (200), (220) and (311) of the face centered cubic (FCC) structure of the metallic silver, according to the Joint Committee on Powder Diffraction Standards of N: 00-004-0783 [25]. It was confirmed that the most intense peak located at $2\theta = 38.15°$ corresponds to diffractions of spherical nanoparticles crystallized in the FCC structure with basal (111) lattice plane. Using the Scherrer equation [28], the crystallite size for the crystallographic plane was estimated as (31.5 ± 2.0) nm.

3.2. Structural and morphological characterization of the $CaSO_4$ samples

Fig. 4 shows X-ray diffraction of the prepared samples, along with the pattern obtained from the ICSD crystallographic database. The formation of a single phase with orthorhombic symmetry of the Amma space group and diffraction peaks and relative intensities corresponding to the anhydride structure were observed.

The crystal surface and morphology were analyzed through the SEM as shown in Fig. 5a. The $CaSO_4$ samples obtained after calcination of the compound show well grained images with quite agglomeration in the grains. These grains have irregular morphology, sizes with particle diameters from 75 μm to 150 μm, due to the grain selection process, prior to the pellet sintering procedure. In order to analyze the behavior of the grains after pressing and sintering of the pellets, SEM micrographs of the surface of the compost pellets were obtained at different magnifications. A homogeneous and cohesive surface can be observed in the SEM micrograph shown in Fig. 5b. The pellets presented also low porosity, as noted in Fig. 5c and d, which were obtained with higher magnification. Low porosity ensures good characteristics for dosimetric applications, since the thermal conductivity of the material increases as long as porosity decreases.

3.3. IR and Raman spectra

The FTIR spectra of *$CaSO_4$:Tb, $CaSO_4$:Tb, Ag and $CaSO_4$:Tb,Ag(NP)* composites are exhibited in Fig. 6. Each spectrum can be divided in four regions. The first region, between 4000 cm^{-1} and 3000 cm^{-1}, presents a broad band centered at about 3449 cm^{-1} corresponding to the absorption due to stretching of OH bands [29]. The second region, between 3000 cm^{-1} and 2000 cm^{-1}, shows two very low intensity bands at 2927 cm^{-1} and 2855 cm^{-1} resulted from the C–H stretching, and two bands at 2244 and 2135 cm^{-1} corresponding to the stretching mode of the carbon-carbon triple bond [30]. It is also possible to see a doublet at 2350 cm^{-1} due to CO_2 stretch [29].

In the third region, covering the range from 2000 cm^{-1} to 1000 cm^{-1}, it is possible to observe vibrational modes of the C═C bond stretching centered at 1640 cm^{-1}, and a deformation mode of the C–H group in 1384 cm^{-1}. The band situated at 1555 cm^{-1} is related to stretching vibration of S═O bonds and the peak at 1090 cm^{-1} is due to the S–O stretching mode [30].

The sulphate bond formation in the samples is also noted in the fourth region, ranged from 1000 cm^{-1}–500 cm^{-1}, by observing the peaks at 950, 679, 613, and 594 cm^{-1}, which are assigned to the stretching and bending modes of bidentate SO_4 [31].

As expected, there are no peaks assigned to silver particles as they are not active in the middle infrared region. On the other hand, the bands corresponding to the O–H group around 3500 cm^{-1} decrease with the incorporation of silver nanoparticles, which indicates that there was a deprotonation of the hydroxyl group. The bands at 2244 cm^{-1} and 2135

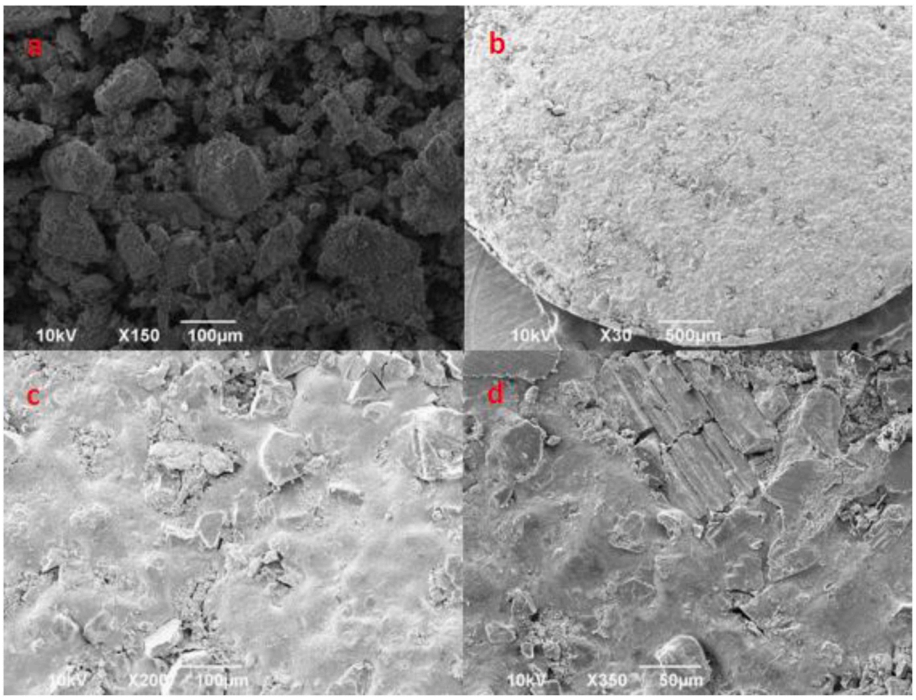

Fig. 5. (a) SEM micrograph of calcined $CaSO_4$ grains using 150X magnification, and micrographs of $CaSO_4$ pellets obtained at different magnifications (b) 30×, (c) 200X, and (d) 350X.

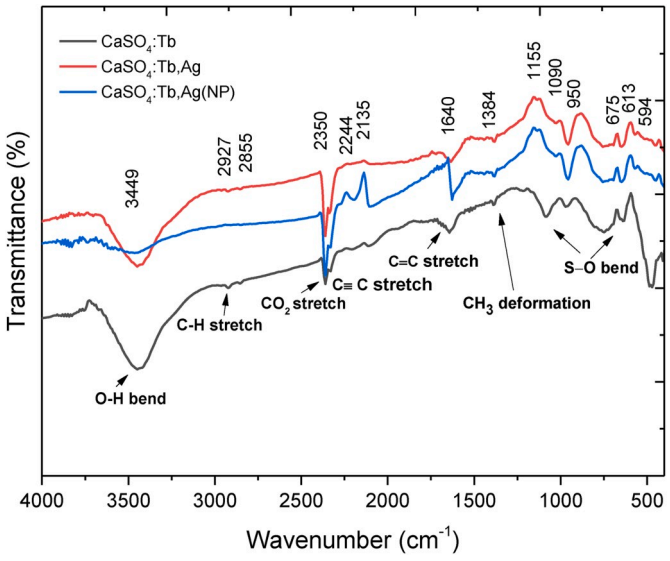

Fig. 6. FTIR spectra of $CaSO_4$:Tb,$CaSO_4$:Tb, Ag and $CaSO_4$:Tb,Ag(NP).

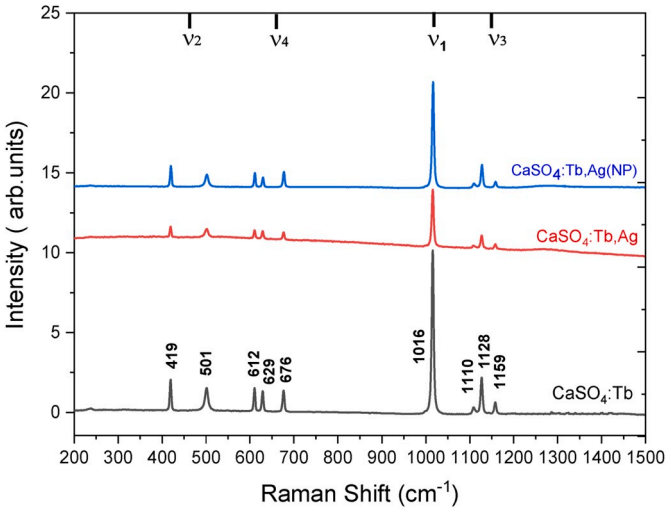

Fig. 7. Room-temperature Raman spectra of $CaSO_4$:Tb, $CaSO_4$:Tb, Ag and $CaSO_4$:Tb,Ag(NP) over the whole optical frequency range. The normal-mode frequencies of the free SO_4 ion are indicated on the top frequency axis by ν_1, ν_2, ν_3, and ν_4.

cm^{-1}, that represent C–C stretch of alkynes, presented an increase in the peak with a decrease of the band intensity in the FTIR spectrum of the $CaSO_4$:Tb,Ag(NP) samples. Other significant differences can be also observed in these spectra at the 1640 cm^{-1} band, which corresponds to C–C stretch of alkenes, and at the 1155 cm^{-1} band, which corresponds to the S–O stretch. The differences may be the result of the interaction of these compounds with the NPs or with another component of the extract itself.

The Raman spectra of the samples, showed in Fig. 7, are similar, indicating no substantial differences among $CaSO_4$:Tb, $CaSO_4$:Tb, Ag and $CaSO_4$:Tb,Ag(NP). This indicates that there were no variations in the chemical bonds of these samples. However, there was a reduction in the peak intensities for the silver codoping materials. This may be associated with defects found in the crystal lattice.

It is important to notice that the peaks observed in the Raman spectra of these composites refer only to the tetrahedron vibration modes of SO_4. The strongest peak, at 1016 cm^{-1}, corresponds to the υ_1 symmetric stretch vibration mode of SO_4 tetrahedra. The less intense peaks at 419 cm^{-1} and 501 cm^{-1} are attributed to the ν_2 symmetric bending, and the peaks at 612 cm^{-1}, 629 cm^{-1} and 676 cm^{-1} are attributed to ν_4 anti-symmetric bending. Finally, the peaks at 1110 cm^{-1}, 1128 cm^{-1}, 1159 cm^{-1} correspond to the ν_3 antisymmetric stretch vibration modes [32]. Thus, all of the peak assignments indicate the presence of anhydride phases in the samples, and thus confirm the identity of the compounds, in accordance with the XRD analyses.

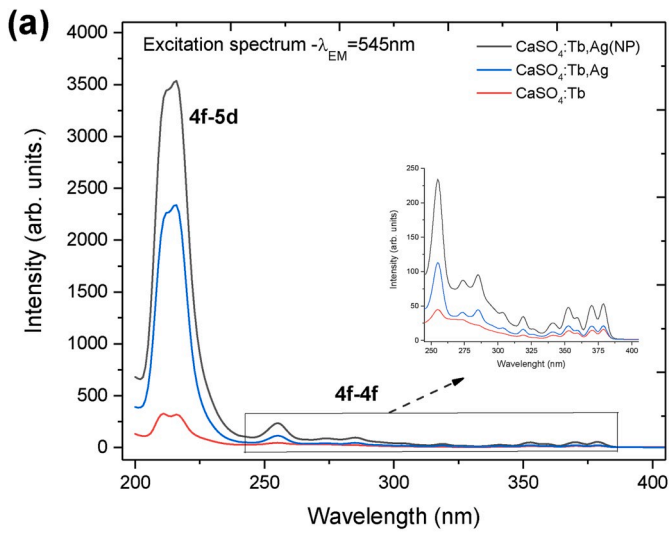

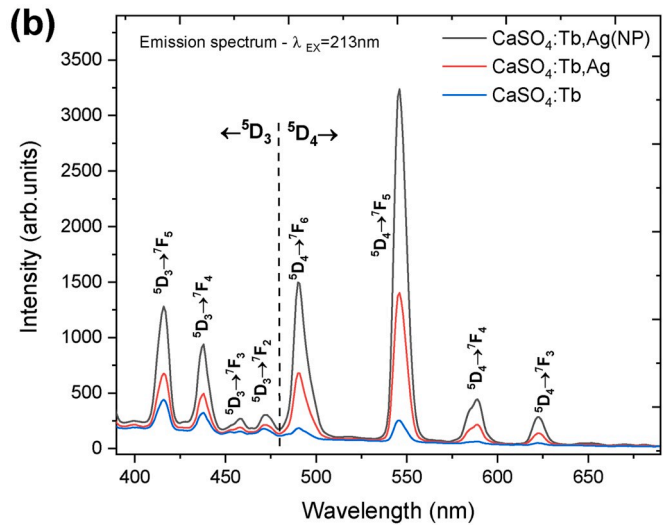

Fig. 8. The excitation (a) and emission (b) spectra of $CaSO_4$:Tb, $CaSO_4$:Tb, Ag and $CaSO_4$:Tb,Ag(NP).

3.4. 3.4. Photoluminescence studies

Fig. 8 shows the excitation and emission spectra of $CaSO_4$:Tb, $CaSO_4$:Tb,Ag(NP) and $CaSO_4$:Tb, Ag.The excitation spectra monitored at 545 nm show a broad band ranging from 200 nm to 240 nm with the maximum at ~ 213 nm, which results from 4f-5d spin-allowed transitions of the Tb^{3+} ion. Other weak absorption bands in the region of 240 nm–350 nm are attributed to 4f-4f spin-forbidden transitions [33].

The photoluminescence emission spectra when excited at 213 nm exhibits $4f^8 \rightarrow 4f^8$ transitions in two regions. The emissions in the green region are assigned to the $^5D_4$ to ^7F_J (J = 6,5,4,3) transitions related to emission peaks at 485, 545, 590 and 620 nm. In the blue region, the $^5D_3$ to ^7F_J transitions cover the spectral range of 400–485 nm [33].

Through these spectra, it is also possible to observe that the addition of silver to the trivalent terbium ion provided an improvement in the photoluminescent properties, which resulted in a significant increase in the luminescent intensity. This means that silver mainly in nanoparticle form was able to generate structure defects more satisfactorily, possibly acting as an energy transfer ion.

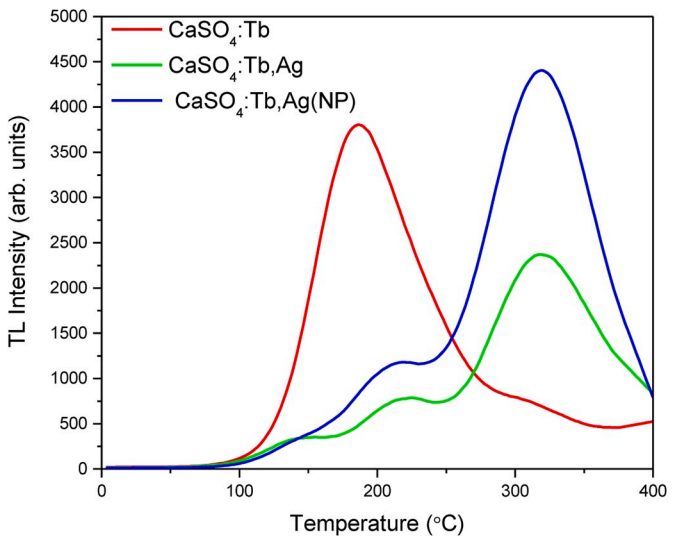

Fig. 9. TL glow curves of samples of $CaSO_4$:Tb,$CaSO_4$:Tb, Ag and $CaSO_4$:Tb,Ag (NP), after irradiation of 1 Gy ($^{90}Sr+^{90}Y$). A heating rate of 10 °C/s was used.

3.5. Thermoluminescence studies

3.5.1. Thermoluminescence glow curve

Fig. 9 shows the TL glow curves of $CaSO_4$:Tb, $CaSO_4$:Tb,Ag, and $CaSO_4$:Tb,Ag(NP) samples obtained after irradiation with an absorbed dose of 1 Gy from the beta source ($^{90}Sr/^{90}Y$) of the Risø TL/OSL reader. The $CaSO_4$:Tb samples presented a main dosimetric peak at approximately 185 °C (resulting from the overlapping of two intense peaks around 178 °C and 212 °C, as shown in Fig. 10, which presents the TL glow curve deconvolution of the produced samples using the CGCD method) and a low intensity peak around 300 °C. It is also possible to observe a shoulder of a peak over 400 °C. Samples codoped with silver presented peaks around 140 °C, 205 °C and 315 °C (resulting from the overlapping of two intense peaks around 310 °C and 357 °C). It is very clear that the codoping of the $CaSO_4$:Tb matrix with silver changes the TL emission of the compounds, due to the addition of recombination centers located at deeper levels. It may also be noted from Fig. 9 that the TL emission of $CaSO_4$:Tb,Ag(NP) is more intense than the $CaSO_4$:Tb, Ag TL emission. It suggests that the nanoparticles are creating more traps for electrons in the band gap of the material. The same behavior was reported by Junot et al. [10] for $CaSO_4$ samples doped with europium and silver nanoparticles. In section 3.5.4 is presented a discussion on the possible luminescent mechanisms resulting from the Ag insertion into the $CaSO_4$:Tb matrix.

Table 1 shows the TL parameters of the produced samples obtained by means of the CGCD method, using the Glow Fit program. The program reported FOM values of 3.50%, 1.39% and 0.77% for the fittings of the $CaSO_4$:Tb, $CaSO_4$:Tb, Ag and $CaSO_4$:Tb,Ag(NP) samples, respectively. The peak temperatures (T_m), the maximum peak intensities (I_m) and the activation energies (E) are reported in Table 1. As can be seen, for the $CaSO_4$:Tb samples the greatest I_m and E are found to be related to peaks 1 and 2. On the other hand, for the $CaSO_4$:Tb, Ag and $CaSO_4$:Tb,Ag (NP) samples, the greatest I_m and E are found to be related to peaks 3 and 4, with higher T_m.

3.5.2. TL reproducibility, response and sensitivity

Fig. 11 presents the variation of the TL response (area under the whole curve) of the samples over five cycles of irradiation, reading and heat treatment. Each point represents the average values of the TL readings of 5 pellets, and the bars represent their standard deviations. It was possible to verify that the response of all samples after every cycle was similar, with variations smaller than 8%. Therefore, it can be stated that the TL signal from the produced samples is reproducible.

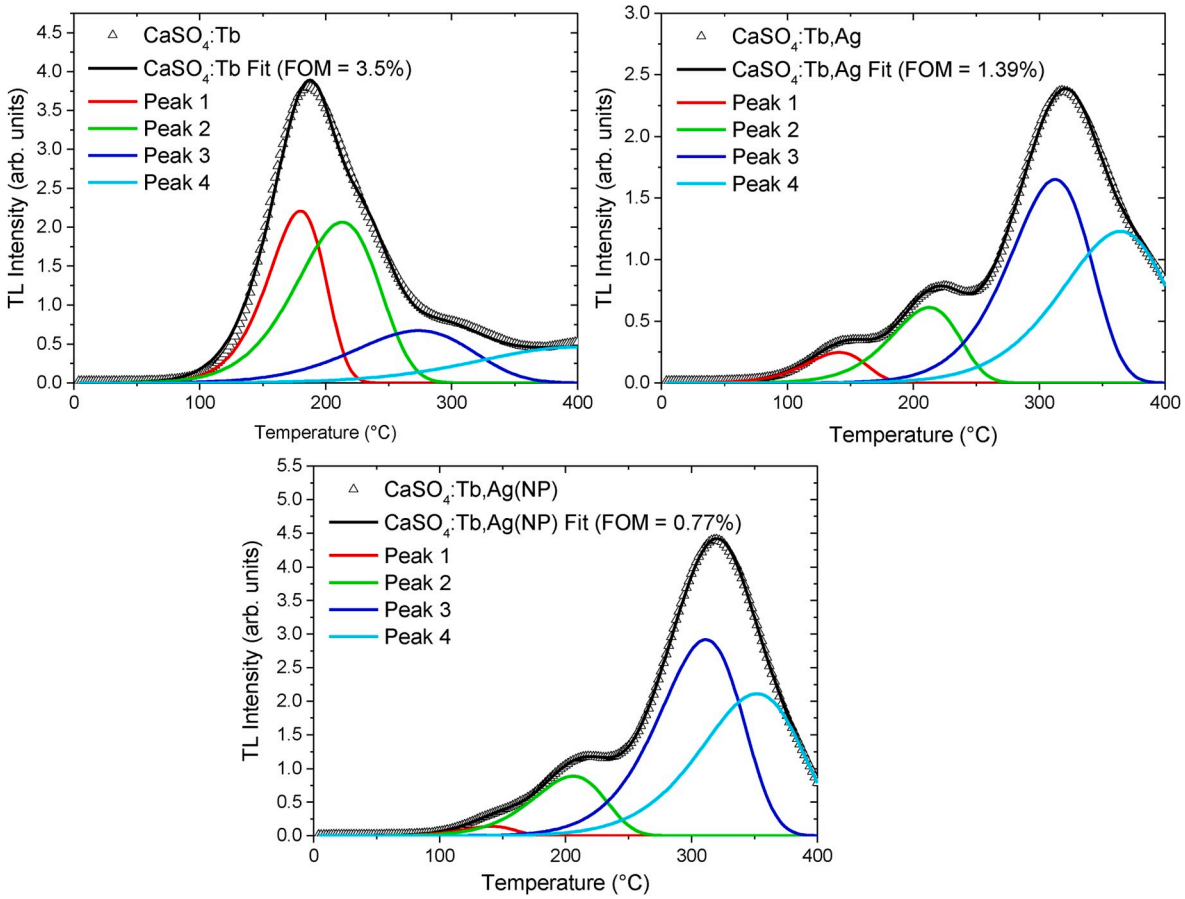

Fig. 10. TL glow curve deconvolution of samples of CaSO4:Tb, CaSO4:Tb, Ag and CaSO4:Tb,Ag(NP) using the CGCD method.

Table 1
TL parameters of the produced samples obtained by means of the CGCD method.

SAMPLE	FOM (%)	Peak	T_m (K)	I_m (arb.units)	E (eV)
$CaSO_4$:Tb	3.50	1	451.77 ± 0.01	2207.99 ± 5.45	0.76 ± 0.01
		2	485.24 ± 0.07	2064.69 ± 6.18	0.63 ± 0.01
		3	540.87 ± 0.22	768.82 ± 11.44	0.47 ± 0.01
		4	700.00 ± 3.98	534.14 ± 4.60	0.41 ± 0.02
$CaSO_4$:Tb,Ag	1.39	1	414.17 ± 0.04	247.59 ± 0.34	0.59 ± 0.01
		2	485.79 ± 0.02	611.93 ± 0.86	0.71 ± 0.01
		3	585.72 ± 0.01	1650.35 ± 17.26	0.88 ± 0.01
		4	637.53 ± 0.54	1228.99 ± 6.15	0.79 ± 0.01
$CaSO_4$:Tb,Ag (NP)	0.77	1	414.11 ± 0.06	140.15 ± 0.42	0.68 ± 0.02
		2	479.04 ± 0.02	886.40 ± 0.55	0.65 ± 0.01
		3	584.35 ± 0.03	2917.36 ± 33.34	0.85 ± 0.02
		4	624.95 ± 0.54	2112.28 ± 19.19	0.80 ± 0.07

In order to investigate the linearity of TL response, the samples were irradiated at increasing doses from 169 mGy to 10 Gy. A linear adjustment was performed to verify the linearity range of the response. The adjustments presented an almost linear correlation coefficients of 0.993 for $CaSO_4$:Tb, 0.998 for $CaSO_4$:Tb, Ag and 0.993 for $CaSO_4$:Tb,Ag(NP) samples. It can be observed in Fig. 12 that the dose-response curves of the composites show a slightly linear behavior in the tested dose range.

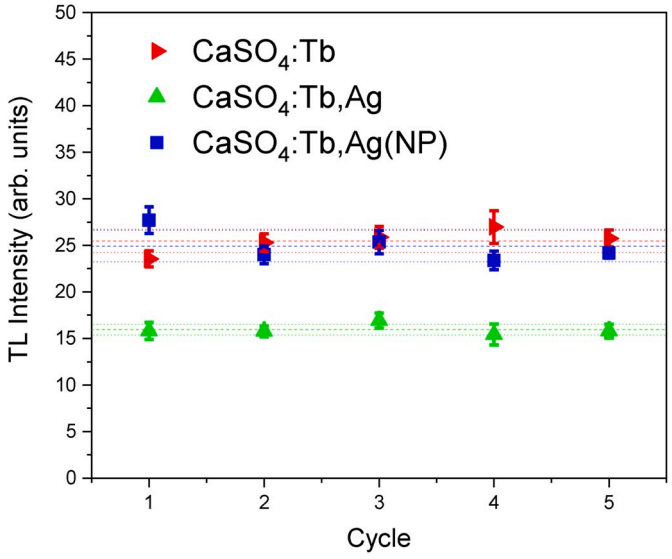

Fig. 11. TL response (integrated area) of samples of $CaSO_4$:Tb, $CaSO_4$:Tb, Ag and $CaSO_4$:Tb,Ag(NP) after each irradiation/reading/heat treatment cycle.

Using the ratio between TL response and absorbed dose, it can be observed that the samples showed TL sensitivity in the same order of magnitude. However, the $CaSO_4$:Tb,Ag(NP) and $CaSO_4$:Tb composites

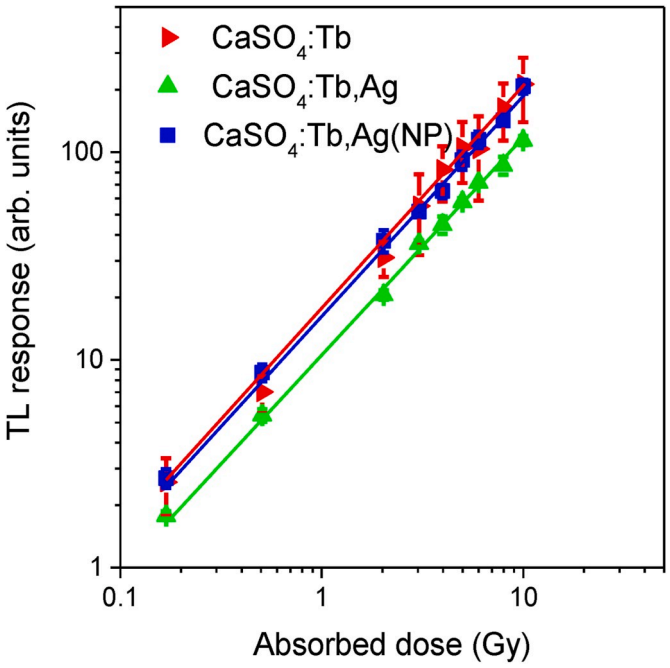

Fig. 12. TL dose-response curves (integrated area) of samples of $CaSO_4$:Tb, $CaSO_4$:Tb, Ag and $CaSO_4$:Tb,Ag(NP).

Table 2
LDD of the compounds produced and their uncertainties for the TL technique.

SAMPLE	$\overline{B}$ (a.u.)	$\sigma_{\overline{B}}$ (a.u.)	f_c (mGy/a.u.)	LDD (mGy)
$CaSO_4$:Tb	1769.0	147.0	4.70×10^{-3}	**10.51 ± 0.06**
$CaSO_4$:Tb,Ag	1828.0	333.2	8.80×10^{-3}	**24.95 ± 0.15**
$CaSO_4$:Tb,Ag(NP)	1869.6	94.2	5.00×10^{-3}	**10.86 ± 0.04**

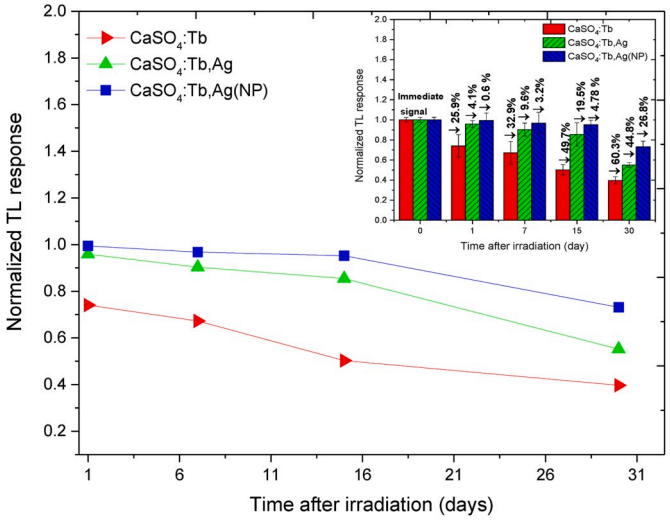

Fig. 13. Normalized TL response of $CaSO_4$:Tb, $CaSO_4$:Tb, Ag and $CaSO_4$:Tb,Ag (NP) samples, presented together with the percentage of fading in different storage time intervals, after a previous irradiation with 1 Gy ($^{90}Sr/^{90}Y$).

presented a sensitivity about 2 times higher than the $CaSO_4$:Tb, Ag composite. Besides that, the $CaSO_4$:Tb samples presented a standard deviation about 4 times higher than the $CaSO_4$:Tb, Ag and $CaSO_4$:Tb,Ag (NP) samples.

3.5.3. Lowest detectable dose (LDD) and fading

The LDD of materials produced was obtained using the equation proposed by Oberhofer e Scharmann [34]:

$$LDD = (\overline{B} + 3\sigma_{\overline{B}})f_c$$

where $\overline{B}$ is the average of the response TL or OSL of the non-irradiated dosimeters of each group; $\sigma_{\overline{B}}$ is the standard deviation of the measures of non-irradiated dosimeters, and f_c is a calibration factor that represents the inverse of the slope of the line of TL/OSL response to absorbed dose. Table 2 shows the lowest detectable doses by the samples irradiated with $^{90}Sr/^{90}Y$, with LDDs of the order of tens of mGy.

Using the total integrated areas of the glow curves, the reduction of the TL responses of the samples were investigated after a previous irradiation with 1 Gy ($^{90}Sr+^{90}Y$) over a period of one day, 7 days, 15 days and 30 days at room temperature and under light protection. Fading results can be seen in Fig. 13.

The dosimetric peak at approximately 185 °C of $CaSO_4$:Tb fades up to 25.9% of the total peak intensity just on the first day of the storage period, whereas on the seventh and fifteenth days, the TL signal faded up to 32.9% and 49.7% of the total peak intensity, respectively. After 30 days, the glow curve showed a 60.3% fading of its original value.

In case of $CaSO_4$:Tb, Ag phosphor, the total TL peak signal decayed 4.1% in one day, 9.6% in 7 days and 19.5% in 15 days. The decay after 30 days seemed to be faster, exhibiting a reduction of 44.8% from the original signal. For $CaSO_4$:Tb,Ag(NP), the TL signal decayed slowly in the first 15 days, exhibiting a reduction of 0.6% in 1 day, 3.2% in 7 days and 4.78% in 15 days. After 30 days, these samples exhibited a reduction of 26.8% in their TL signal.

Samples codoped with silver presented a lower fading, mostly due to their TL peaks at higher temperatures (210 °C and 315 °C), over the whole storage period. High temperature TL peaks are more stable than low-temperature peaks, because shallow traps can be released more easily by thermal stimulation than traps with higher activation energies [35].

3.5.4. TL emission spectra

With the purpose of determining the recombination centers that give rise to the TL emission, the TL emission spectra of the $CaSO_4$:Tb, $CaSO_4$: Tb, Ag and $CaSO_4$:Tb,Ag(NP) samples after a previous irradiation with a $^{90}Sr/^{90}Y$ source (100 Gy) were obtained, and they are shown in Fig. 14. The emissions of the Tb^{3+} ions, with the main emission at 544 nm ($^5D_4 \rightarrow {}^7F_5$), and less intense emissions at 412 nm ($^5D_3 \rightarrow {}^7F_5$), 435 nm ($^5D_3 \rightarrow {}^7F_4$), 488 nm ($^5D_4 \rightarrow {}^7F_6$), 586 nm ($^5D_4 \rightarrow {}^7F_4$) and 620 nm ($^5D_4 \rightarrow {}^7F_3$) can be observed for the three composites. All samples showed green color during heating, consistent with the main emission at 544 nm. It is clear to notice, from Fig. 14, that these spectra presented only divergences in the TL emission curves, as already observed in Fig. 9. Therefore, silver particles do not interfere in the recombination centers of these samples, being only responsible for generating deeper capture centers, with higher activation energies. In the $CaSO_4$:Tb material, Ca^{2+} vacancies are created by the incorporation of Tb^{3+} ion, as well as the sulphate radical related hole traps stabilized by these vacancies. Although the electronic configuration of Ag allows single or double valence, Madhusoodanan et al. [36] clarified that it enters as Ag^+ in the Ca^{2+} site of the $CaSO_4$:Tm^{3+} lattice, and it has been shown that the hole trap in the $CaSO_4$:Ag, RE (RE = Dy, Tm, Tb and Ce) phosphors is characteristic of the Ag^+ ion [37]. Therefore, upon codoping with an Ag^+ ion, local charge compensation occurs when Tb^{3+} ion replaces the Ca^{2+} ion, and the Ca^{2+} vacancies are not created. When the samples are thermally stimulated, recombination of the holes released from Ag^+ ions may occur in electron traps and the recombination energy excites the Tb^{3+} ions. This results in a TL emission characteristic of Tb^{3+} as observed in the emission spectra. Since a significant number of Tb^{3+} ions replaced by Ag^+ ions occurs, there is a reduction of the Tb^{3+} emission, and, consequently, a less intense TL emission is observed for the $CaSO_4$:

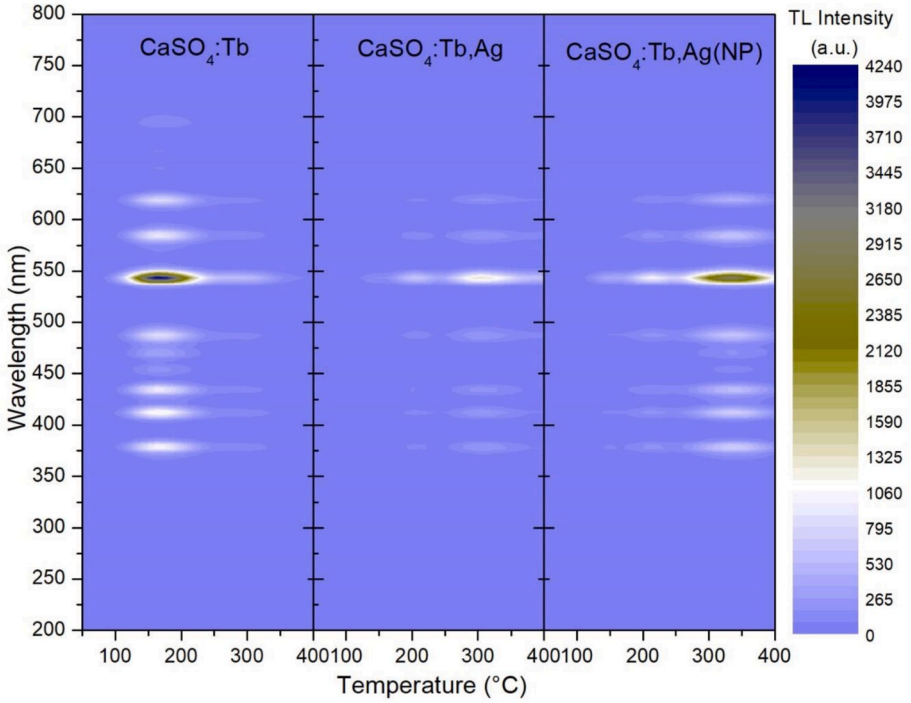

Fig. 14. TL emission spectra of $CaSO_4$:Tb, $CaSO_4$:Tb, Ag and $CaSO_4$:Tb,Ag(NP) samples, after irradiation with 100 Gy ($^{90}Sr/^{90}Y$).

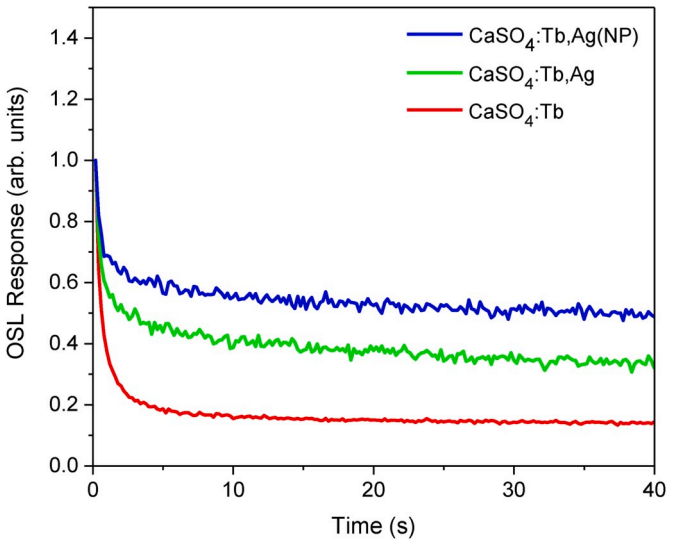

Fig. 15. Typical OSL response of $CaSO_4$:Tb, $CaSO_4$:Tb, Ag and $CaSO_4$:Tb,Ag (NP) samples, after irradiation of 1 Gy ($^{90}Sr/^{90}Y$).

Tb, Ag samples. However, this intensity reduction is compensated when $CaSO_4$:Tb is doped with Ag^0 particles, which may create interstitial defects in the crystal lattice, and then more electron traps. Once the presence of Ag shifts the $CaSO_4$:Tb main TL peak to higher temperatures, it should be very interesting to verify the influence of the concentration of the silver particles in the peak displacement.

3.6. Optically stimulated luminescence studies

3.6.1. OSL decay curves

Fig. 15 presents the OSL curves of the samples produced and irradiated with 1 Gy, obtained in continuous mode (CW), with an integration time of 40 s. All the samples presented a typical exponential decay, proving that the traps are being emptied during the optical stimulation.

Table 3
OSL parameters of the exponential fitted curves of the compounds produced.

SAMPLE	CW-OSL Component	Coefficient A_i	Decay constant t_i (s)
$CaSO_4$:Tb	Fast	1.21 ± 0.02 (A_1)	0.24 ± 0.01 (t_1)
	Medium	0.33 ± 0.01 (A_2)	1.62 ± 0.05 (t_2)
	Slow	0.16 ± 0.01 (A_3)	192.82 ± 8.79 (t_3)
$CaSO_4$:Tb,Ag	Fast	0.90 ± 0.06 (A_1)	0.25 ± 0.02 (t_1)
	Medium	0.18 ± 0.01 (A_2)	3.18 ± 0.35 (t_2)
	Slow	0.43 ± 0.01 (A_3)	152.67 ± 8.94 (t_3)
$CaSO_4$:Tb,Ag (NP)	Fast	0.64 ± 0.05 (A_1)	0.27 ± 0.03 (t_1)
	Medium	0.13 ± 0.01 (A_2)	3.93 ± 0.57 (t_2)
	Slow	0.56 ± 0.01 (A_3)	313.50 ± 32.02 (t_3)

However, the behavior of the OSL emission curve of $CaSO_4$:Tb differs from the other composites. These samples present an initial predominance of a fast decay rate, which results from the direct recombination between the electrons and holes in the luminescent centers. The OSL signals of the $CaSO_4$:Tb, Ag and $CaSO_4$:Tb,Ag(NP) samples show the predominance of slow decay rates due to the recapture of the charges that are released from the deeper traps by shallower traps prior to recombination. This is due to the incorporation of silver in the matrix. It is noteworthy that the stimulation wavelength of the blue LEDs (470 nm) did not have enough energy to stimulate the traps at deeper energies (for the TL peak temperature range at 250–400 °C), resulting in a low photoionization cross-section for samples codoped with silver. The same behavior was observed in samples of $CaSO_4$:Tm, Ag [38].

The decay behaviors of the experimental OSL curves were fitted using a three-component exponential function:

$$I_{OSL} = A_1 e^{-t/\tau_1} + A_2 e^{-t/\tau_2} + A_3 e^{-t/\tau_3}$$

where I_{OSL} is the OSL intensity; A_1, A_2, and A_3 are constant coefficient; and τ_1, τ_2, and τ_3 are the decay constants related to the different sets of traps [39,40]. Table 3 shows the parameters obtained from an exponential fitting of the OSL decay curves presented in Fig. 16. As can be observed, the greatest value of A_1 (1.2188) was reached for the $CaSO_4$:Tb samples, confirming the predominance of the fast component (τ_1 =

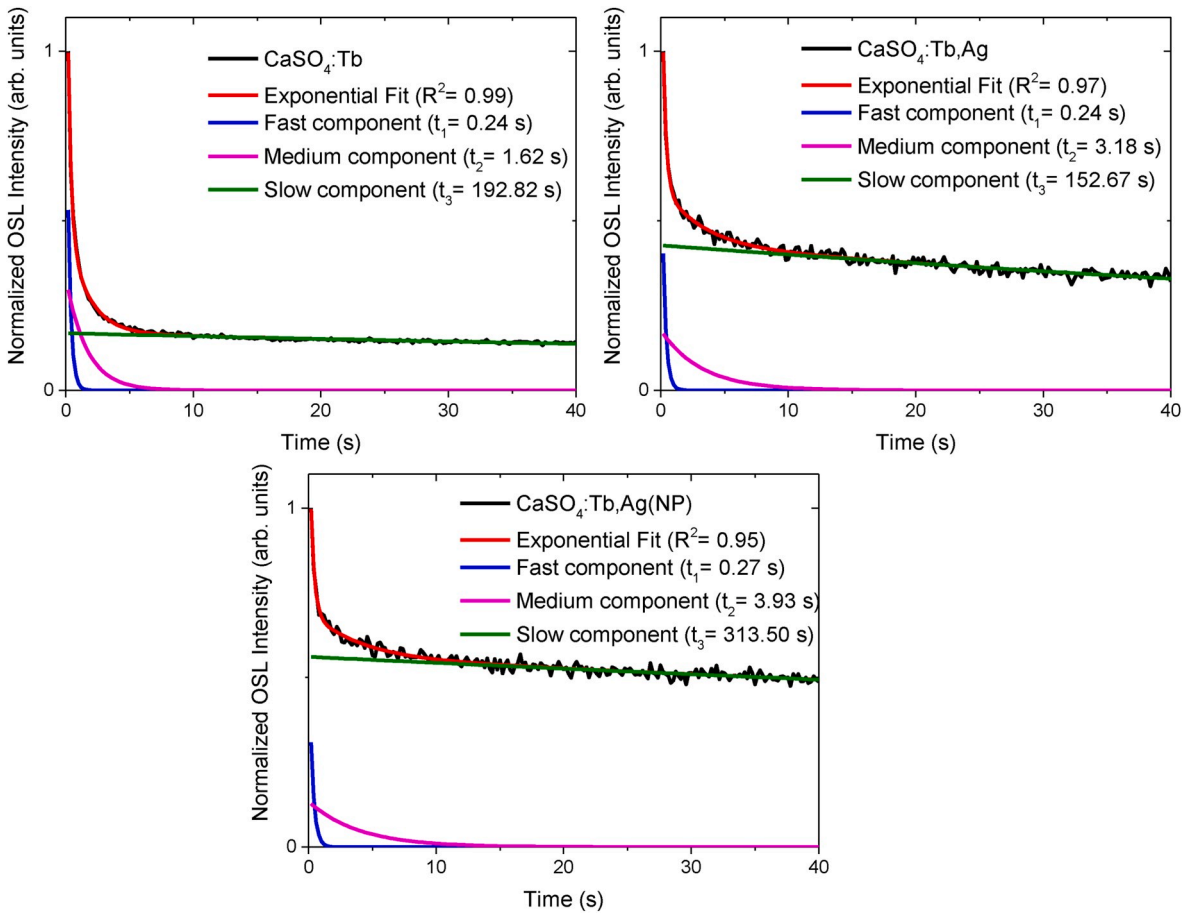

Fig. 16. Experimental and fitted OSL decay curves for CaSO4:Tb, CaSO4:Tb, Ag and CaSO4:Tb,Ag(NP) samples.

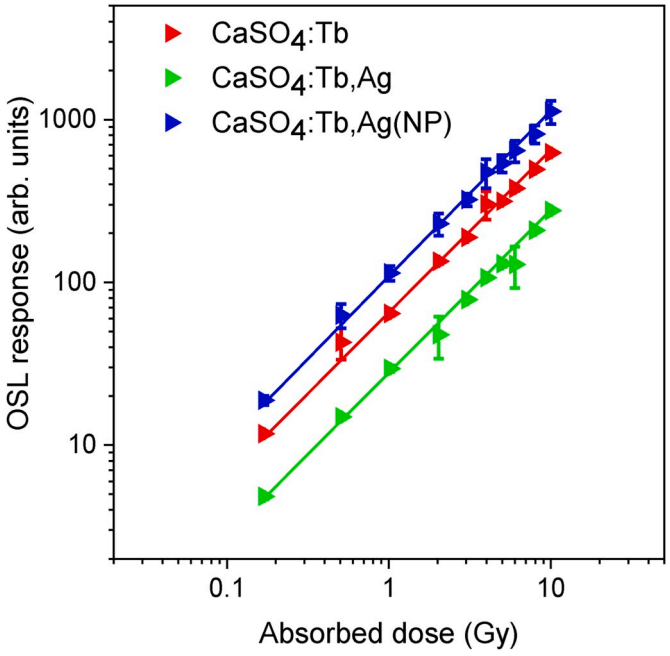

Fig. 17. OSL response (integrated area) of the samples of CaSO4:Tb, CaSO4:Tb, Ag and CaSO4:Tb,Ag(NP) samples as a function of the absorbed dose of beta radiation (90Sr/90Y).

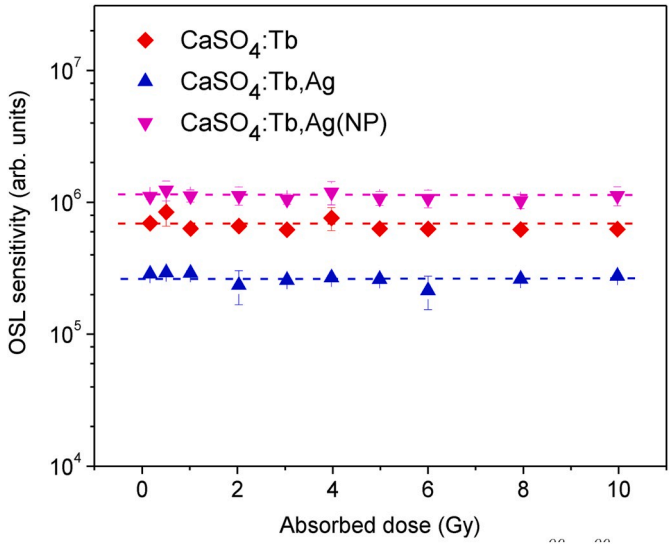

Fig. 18. OSL sensitivity of the pellets when exposed to $^{90}Sr/^{90}Y$ beta radiation.

0.24 s) in these samples. The slow component is prevalent for the $CaSO_4$:Tb,Ag(NP) samples; its fit resulted in $A_3 = 0.5609$ and a lifetime of $\tau_3 = 313.5$ s. Experimental and fitted OSL glow curves, as well as their separate exponential terms, are shown in Fig. 16. A good agreement may be observed between applied fitting and experimental result.

Table 4
LDD of the compounds produced and their uncertainties for the OSL technique.

DETECTOR	$\overline{B}$ (a.u.)	$\sigma_{\overline{B}}$ (a.u.)	f_c (mGy/a.u.)	LDD (mGy)
$CaSO_4$:Tb	5537.8	539.8	0.0016	**11.53 ± 0.53**
$CaSO_4$:Tb,Ag	7429.0	299.5	0.0009	**31.44 ± 0.29**
$CaSO_4$:Tb,Ag(NP)	9527.2	320.9	0.0037	**9.67 ± 0.32**

3.6.2. OSL response and OSL sensitivity

A slightly linear behavior of the OSL intensity of the samples studied as a function of the absorbed dose for the range from 169 mGy to 10 Gy is observed in Fig. 17. The linear adjustment performed presented linear correlation coefficients of 0.996 for $CaSO_4$:Tb, 0.992 for $CaSO_4$:Tb, Ag and 0.997 for $CaSO_4$:Tb,Ag(NP).

The experimental results of the average luminescent sensibility to the absorbed dose are shown in Fig. 18 in a semi-log plotted graph. The evaluated samples presented OSL sensitivity in the same order of magnitude, but the sensitivity of the $CaSO_4$:Tb,Ag(NP) samples is 4 times higher compared to the $CaSO_4$:Tb, Ag samples and 1.5 times higher compared to the $CaSO_4$:Tb samples.

3.6.3. Lowest detectable dose (LDD)

In the present study, LDD values for all the samples were determined as described in Section 3.5.3. They were also calculated through the OSL measurements, and they are presented in Table 4 together with the mean values and standard deviations of the OSL response of the non-irradiated dosimeters and the calibration factor.

According to Table 4, the LDDs of the samples are in the same order of magnitude of mGy. The $CaSO_4$:Tb,Ag(NP) shows a lowest detection limit about 3 times lower than $CaSO_4$:Tb,Ag.

3.6.4. Correlation between the TL and OSL emissions

Fig. 19 shows the results obtained from the consecutive measurements (TL→ OSL and OSL → TL) of the $CaSO_4$:Tb, $CaSO_4$:Tb, Ag and $CaSO_4$:Tb,Ag(NP) samples. The previous TL measurements of $CaSO_4$:Tb, Ag and $CaSO_4$:Tb,Ag(NP) samples bring about the OSL signal to background levels in samples, indicating that all the OSL traps are completely emptied after the TL emission. While the $CaSO_4$:Tb samples showed a low intensity OSL decay curve, indicating that part of these traps is not completely emptied, responding to optical stimulation.

It was also observed that the previous OSL reading interferes with the

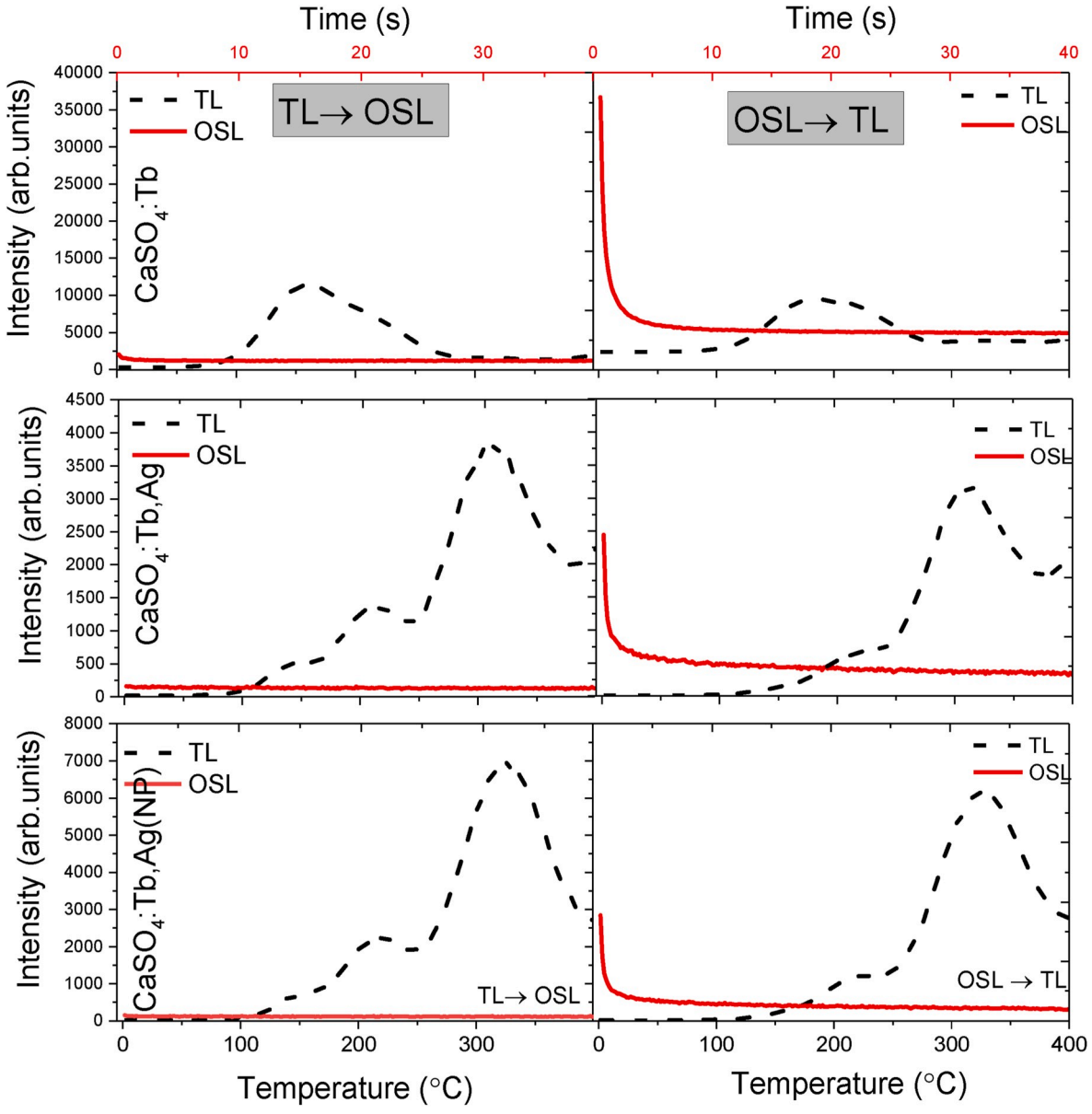

Fig. 19. TL-OSL and OSL-TL responses of the $CaSO_4$:Tb, $CaSO_4$:Tb,Ag, and $CaSO_4$:Tb,Ag(NP) samples.

result of the subsequent reading of the TL signal. For the $CaSO_4$:Tb it is possible to notice that the traps that give rise to the 185 °C peak have a low photoionization cross section, once its TL intensity reduced only in 44%, even after the optical stimulation. For $CaSO_4$:Tb, Ag and $CaSO_4$:Tb, Ag(NP) samples, it is noted that the traps that give rise to the low intensity peaks, around 135 °C and 210 °C, present a higher photoionization cross section than the traps that give rise to the 315 °C peak, once its TL intensity presented just a small decrease even after the optical stimulation with 470 nm light from the blue LEDs. This indicates that the fast decay of the OSL emission of these samples is mostly due to shallow traps. Besides that, the recombination centers responsible for the OSL emission are distinct from those centers responsible for the TL emission.

4. Conclusions

The formation of the silver nanoparticles used as codopants in the $CaSO_4$ matrix was confirmed by the color change throughout the synthesis process. XRD analyses indicated the crystalline FCC structure of the prepared AgNPs, estimating the mean crystallite size as (31.5 ± 2.0) nm. The UV–Vis spectrum presented a plasmon resonance band with the maximum around 425 nm, characteristic of AgNPs. SEM images showed irregular grain morphology and homogeneous pellets, with a cohesive surface and a low degree of porosity. The FTIR spectra showed bands around 1155 cm^{-1} e 1090 cm^{-1} and in the range of 950–594 cm^{-1}, that are characteristic of those reported in the literature for sulphate ions, which confirms the formation of a sulphate bond in the samples. The characteristic bands around 3349 cm^{-1} and 2350 cm^{-1} are attributed to water vapor and atmospheric CO^2; this indicates that the prepared sample consists of a certain amount of moisture. Other vibrational frequencies observed in the spectra are attributed to hydrocarbons (alkanes and alkynes). Raman spectra showed nine vibrational modes, corresponding to SO_4 tetrahedron vibrational modes. Luminescent measurements revealed characteristic emissions of Tb^{3+}. Through these spectra a significant increase in the transition intensity was also observed adding silver as codopant, mainly in the nanoparticle form.

The addition of silver as a codopant in the $CaSO_4$:Tb matrix allows a shift of the dosimetric peak to a higher temperature (310 °C), and the presence of silver particles at the nanoscale increases the TL emission intensity of this phosphorus, creating more traps for the electrons. This increase in intensity may represent a greater interest in the use of $CaSO_4$:Tb,Ag(NP) in TL dosimetry. The TL emission spectra confirmed the incorporation of the Tb^{3+} ion into the calcium sulphate matrix. In the case of the OSL response, the phosphors presented a typical exponential decay curve, with the rapid component predominance changed to the very slow component predominance when incorporating the silver in the $CaSO_4$:Tb matrix; the best OSL response was that of samples without silver incorporation. All the studied samples presented TL and OSL signals reproducible and linear in the employed dose range and the lowest detectable dose was of the order of mGy. $CaSO_4$:Tb,Ag(NP) presented a higher sensitivity to radiation than $CaSO_4$:Tb, Ag and $CaSO_4$:Tb, denoting its potential use as an TL/OSL dosimeter.

CRediT authorship contribution statement

Anderson M.B. Silva: Conceptualization, Methodology, Investigation, Writing - original draft. **Danilo O. Junot:** Data curation, Investigation, Writing - review & editing. **Linda V.E. Caldas:** Conceptualization, Visualization, Resources. **Divanizia N. Souza:** Supervision, Writing - original draft, Project administration.

Acknowledgments

The authors thank the Brazilian agencies Coordenação de Aperfeiçoamento de Pessoal de Nível Superior - (CAPES) – Project 23038.007416/2012–79, and Conselho Nacional de Desenvolvimento Científico e Tecnológico - Brazil (CNPq) - Grants 150678/2017-7, 301335/2016–8, 308090/2016-0, and Comissão Nacional de Energia Nuclear.

References

[1] K.S.V. Nambi, V.N. Bapat, A.K. Ganguly, Thermoluminescence of $CaSO_4$ doped with rare earths, J. Phys. C Solid State Phys. 7 (1974) 4403–4415.
[2] T. Yamashita, N. Nada, H. Onishi, S. Kitamura, Calcium sulfate activated by thulium or dysprosium for thermoluminescence dosimetry, Health Phys. 21 (1971) 295–300.
[3] M. Prokić, Improvement of the thermoluminescence properties of the non-commercial dosimetry phosphors $CaSO_4$:Dy and $CaSO_4$:Tm, Nucl. Instrum. Methods 151 (1978) 603–608.
[4] A.R. Lakshmanan, Photoluminescence and thermostimulated luminescence processes in rare-earth-doped CaSO4 phosphors, Prog. Mater. Sci. 44 (1999) 1–187.
[5] N.B. Ingle, S.K. Omanwar, P.L. Muthal, S.M. Dhopte, V.K. Kondawar, T. K. Gundurao, S.V. Moharil, Synthesis of $CaSO_4$:Dy, $CaSO_4$:Eu^{3+} and $CaSO_4$:Eu^{2+} phosphors, Radiat. Meas. 43 (2008) 1191–1197.
[6] D.O. Junot, J.P. Barros, L.V.E. Caldas, D.N. Souza, Thermoluminescent analysis of CaSO4:Tb,Eu crystal powder for dosimetric purposes, Radiat. Meas. 90 (2016) 228–232.
[7] M.G. Nunes, L.L. Campos, Study of $CaSO_4$:Dy and LiF:Mg,Ti detectors TL response to electron radiation using a SW Solid Water phantom, Radiat. Meas. 43 (2008) 459–462.
[8] M.A.P. Chagas, M.G. Nunes, L.L. Campos, D.N. Souza, TL properties of anhydrous $CaSO_4$:Tm improvement, Radiat. Meas. 45 (2010) 550–552.
[9] I. Kása, R. Chobola, P. Mell, S. Szakács, A. Kerekes, Preparation and investigation of thermoluminescence properties of $CaSO_4$:Tm,Cu, Radiat. Protect. Dosim. 123 (2006) 32–35.
[10] D.O. Junot, M.A. Couto dos Santos, P.L. Antonio, L.V.E. Caldas, D.N. Souza, Feasibility study of $CaSO_4$:Eu, $CaSO_4$:Eu,Ag and $CaSO_4$:Eu,Ag(NP) as thermoluminescent dosimeters, Radiat. Meas. 71 (2014) 99–103.
[11] B.A. Doull, L.C. Oliveira, D.Y. Wang, E.D. Milliken, E.G. Yukihara, Thermoluminescent properties of lithium borate, magnesium borate and calcium sulfate developed for temperature sensing, J. Lumin. 146 (2014) 408–417.
[12] E.G. Yukihara, A.C. Coleman, B.A. Doull, Passive temperature sensing using thermoluminescence: Laboratory tests using $Li_2B_4O_7$: Cu,Ag, MgB_4O_7:Dy, Li and $CaSO_4$:Ce,Tb, J. Lumin. 146 (2014) 515–526.
[13] E.G. Yukihara, A.C. Coleman, S. Bastani, T. Gustafson, J.J. Talghader, A. Daniels, F. R. Svingala, Particle temperature measurements in closed chamber detonations using thermoluminescence from $Li_2B_4O_7$: Ag,Cu, MgB_4O_7:Dy,Li and $CaSO_4$:Ce,Tb, J. Lumin. 165 (2015) 145–152.
[14] D.O. Junot, D.F. Vasconcelos, M.A.P. Chagas, M.A. Couto dos Santos, L.V.E. Caldas, D.N. Souza, Silver addition in $CaSO_4$:Eu, TL and TSEE properties, Radiat. Meas. 46 (2011) 1500–1502.
[15] M.S. Kulkarni, R.R. Patil, A. Patle, N.S. Rawat, P. Ratna, B.C. Bhatt, S.V. Moharil, Optically stimulated luminescence from $CaSO_4$:Eu - preliminary results, Radiat. Meas. 71 (2014) 95–98.
[16] K.J. Kearfott, W.G. West, M. Rafique, The optically stimulated luminescence (OSL) properties of LiF:Mg,Ti, $Li_2B_4O_7$:Cu, $CaSO_4$:Tm, and CaF_2:Mn thermoluminescent (TL) materials, Appl. Radiat. Isot. 99 (2015) 155–161.
[17] V. Guckan, V. Altunal, N. Nur, T. Depci, A. Ozdemir, K. Kurt, Y. Yu, I. Yegingil, Z. Yegingil, Studying $CaSO_4$:Eu as an OSL phosphor, Nucl. Instrum. Methods Phys. Res. B. 407 (2017) 145–154.
[18] S.K. Omanwar, C.B. Palan, Synthesis and preliminary OSL studies of Ce^{3+} activated calcium sulfate ($CaSO_4$) for radiation dosimetry, J. Mater. Sci. Mater. Electron. 29 (2018) 7388–7392.
[19] M. Yüksel, T. Dogan, Z.G. Portakal, M. Topaksu, Synthesis and luminescence characterization of microcrystalline Nd-doped calcium sulfate, Appl. Radiat. Isot. 148 (2019) 197–203.
[20] S. Bahl, V. Kumar, R.R. Bihari, P. Kumar, Investigations of OSL properties of CaSO4:Mn phosphor exposed to gamma and beta radiations, J. Lumin. 181 (2017) 36–43.
[21] P.C. Lee, D. Meisel, Adsorption and surface-enhanced Raman of dyes on silver and gold sols, J. Phys. Chem. 86 (1982) 3391–3395.
[22] R.A.P.O. D'Amorim, M.I. Teixeira, L.V.E. Caldas, S.O. Souza, Physical, morphological and dosimetric characterization of the Teflon agglutinator to thermoluminescent dosimetry, J. Lumin. 136 (2013) 186–190.
[23] D.T.U. Nutech, Guide to "The Risø TL/OSL Reader", DTU Nutech, Denmark, 2015.
[24] I.O. Polo, D.O. Junot, L.V.E. Caldas, SOL-GEL α-Al_2O_3 samples: analysis of the TL kinetics, J. Appl. Phys. 125 (2019) 185102.
[25] M.A. Raza, Z. Kanwal, A. Rauf, A.N. Sabri, S. Riaz, S. Naseem, Size-and shape-dependent antibacterial studies of silver nanoparticles synthesized by wet chemical routes, Nanomaterials 6 (2016) 74.
[26] D. Kim, S. Jeong, J. Moon, Synthesis of silver nanoparticles using the polyol process and the influence of precursor injection, Nanotechnology 17 (2006) 4019–4024.
[27] D.H. Wang, D.Y. Kim, K.W. Choi, J.H. Seo, S.H. Im, J.H. Park, O.O. Park, A. J. Heeger, Enhancement of donor–acceptor polymer bulk heterojunction solar cell power conversion efficiencies by addition of Au nanoparticles, Angew. Chem. Int. Ed. 50 (2011) 5519–5523.
[28] A.L. Patterson, The Scherrer formula for X- ray particle size determination, Phys. Rev. 56 (1939) 978–982.

[29] I.M. McIntosh, A.R. Nichols, K. Tani, E.W. Llewellin, Accounting for the species-dependence of the 3500 cm^{-1} H_2Ot infrared molar absorptivity coefficient: implications for hydrated volcanic glasses, Am. Mineral. 102 (2017) 1677–1689.
[30] M.S. Bhadane, N. Mandlik, B.J. Patil, S.S. Dahiwale, K.R. Sature, V.N. Bhoraskar, S. D. Dhole, $CaSO_4$:Dy microphosphor for thermal neutron dosimetry, J. Lumin. 170 (2016) 226–230.
[31] M.A. Martin, J.W. Childers, R.A. Palmer, Fourier transform infrared photoacoustic spectroscopy characterization of sulfur-oxygen species resulting from the reaction of SO_2 with CaO and $CaCO_3$, Appl. Spectrosc. 41 (1987) 120–126.
[32] N. Prieto-Taboada, O. Gómez-Laserna, I. Martínez-Arkarazo, M.A. Olazabal, J. M. Madariaga, Raman spectra of the different phases in the $CaSO_4$–H_2O system, Anal. Chem. 86 (2014) 10131–10137.
[33] M. Li, L. Wang, W. Ran, Z. Deng, J. Shi, C. Ren, Tunable luminescence in $Sr_2MgSi_2O_7$: Tb^{3+}, Eu^{3+} phosphors based on energy transfer, Materials 10 (2017) 227.
[34] M. Oberhofer, A. Scharmann, Applied Thermoluminescence Dosimetry, CRC Press, Ispra, 1981.
[35] S.W.S. McKeever, M. Moscovitch, P.D. Townsend, Thermoluminescent Dosimetry Materials: Properties and Uses, Nuclear Technology Publishing, Ashford, 1995.
[36] U. Madhusoodanan, M.T. Jose, A. Tomita, W. Hoffmann, A.R. Lakshmanan, A new thermostimulated luminescence phosphor based on $CaSO_4$:Ag,Tm for applications in radiation dosimetry, J. Lumin. 82 (1999) 221–232.
[37] U. Madhusoodanan, M.T. Jose, A. Tomita, A.R. Lakshmanan, New thermostimulated luminescence phosphors based on $CaSO_4$:Ag, RE. J. Lumin. 87–89 (2000) 1300–1302.
[38] D.O. Junot, A.G. Santos, P.L. Antonio, M.V. Rezende, D.N. Souza, L.V.E. Caldas, Dosimetric and optical properties of $CaSO_4$:Tm and $CaSO_4$:Tm,Ag crystals produced by a slow evaporation route, J. Lumin. 210 (2019) 58–65.
[39] R.A. Barve, R.R. Patil, S.V. Moharil, B.C. Bhatt, M.S. Kulkarni, Optically stimulated luminescence in Cu^+ doped lithium orthophosphate, Phys. B Condens. Matter 458 (2015) 117–123.
[40] J.V.B. Valença, A.C.A. Silva, N.O. Dantas, L.V.E. Caldas, F. d'Errico, S.O. Souza, Optically stimulated luminescence of the $20Li_2CO_3$ – $(X)K_2CO_3$ – $(80 - X)B_2O_3$ glass system, J. Lumin. 200 (2018) 248–253.